

Techniques and software tool for 3D multimodality medical image segmentation

D Yang^a, J Zheng^b, A Nofal^a, JO Deasy^a, IM El Naqa^{a*}

^aDepartment of Radiation Oncology, School of Medicine, Washington University in Saint Louis, MO, 63110, USA;

^bMallinckrodt Institute of Radiology, Washington University in Saint Louis, MO, 63110, USA

ABSTRACT

The era of noninvasive diagnostic radiology and image-guided radiotherapy has witnessed burgeoning interest in applying different imaging modalities to stage and localize complex diseases such as atherosclerosis or cancer. It has been observed that using complementary information from multimodality images often significantly improves the robustness and accuracy of target volume definitions in radiotherapy treatment of cancer. In this work, we present techniques and an interactive software tool to support this new framework for 3D multimodality medical image segmentation. To demonstrate this methodology, we have designed and developed a dedicated open source software tool for multimodality image analysis “MIASYS”. The software tool aims to provide a needed solution for 3D image segmentation by integrating automatic algorithms, manual contouring methods, image preprocessing filters, post-processing procedures, user interactive features and evaluation metrics. The presented methods and the accompanying software tool have been successfully evaluated for different radiation therapy and diagnostic radiology applications.

Keywords: multimodality imaging, image segmentation, informatics tools, active contours, radiotherapy

Disclosure: The authors declare no conflicts of interest.

1. INTRODUCTION

The role of multimodality imaging has witnessed an extraordinary surge in diagnostic and therapeutic radiology for diagnosing, staging, and monitoring treatment response in complex diseases such as atherosclerosis (Rudd *et al.*, 2007) and cancer (King, 2007; Hsu *et al.*, 2007). This has been made possible with the recent evolutionary developments in medical imaging instrumentation technology that allows identifying anatomical structures or functional processes *in vivo*. A comprehensive review that follows the historical developments of multimodality imaging instrumentation for clinical use and its future potential has been recently published (Townsend, 2008).

In modern conformal, intensity modulated image-guided radiotherapy (IGRT) particularly, there is a noticeable value for using multimodality imaging in treatment planning, diagnosis, and staging in different cancer sites. The goal is to achieve improved target definition by incorporating different imaging modalities (computed tomography (CT), magnetic resonance (MR), and 3D ultrasound) as well as improved staging, disease characterization and localization using functional and molecular imaging (positron emission tomography (PET), single photon emission computed tomography (SPECT), magnetic resonance spectroscopy (MRS)). In addition, on-board imaging systems (cone beam CT (CBCT), mega-voltage CT (MVCT)) are currently deployed in many clinics to correct patient setup and improve daily delivery of fractionated radiation treatments. While these advanced imaging modalities have created new opportunities in radiotherapy treatment planning and delivery, they have also presented many technical challenges on how to integrate different modalities information properly affecting visualization, delineation, and related areas (El Naqa, 2008).

Historically, kilovoltage CT (kVCT) has been the standard for treatment planning in 3D conformal or intensity-modulated radiation therapy (IMRT). However, it is well known that there can be significant variability when multiple observers contour target prostate volume (Smith *et al.*, 2007). Several studies indicated that this observer variability could be reduced by combining information from multiple modalities. For instance, researchers in lung cancer reported reduced variability when using CT with PET for target definition (Tolozza *et al.*, 2003; Bradley *et al.*, 2004b). Furthermore, a study of fractionated stereotactic radiotherapy for meningioma patients demonstrated improved target definition by combining physiological information from PET, anatomical structure from CT and soft tissues contrasts

*elnaqa@wustl.edu; phone +1 314 362 0129; fax +1 314 362 8521; radonc.wustl.edu

from MRI, resulting in alterations of the original contour definitions in 73 percent of the cases (Milker-Zabel *et al.*, 2006). However, this visual approach for integrating multimodality imaging information is prone to observer subjectivity and variation. Therefore, in this work we propose methods for integrating multimodality imaging information by extending automated and semi-automated segmentation methods into an interactive multimodality framework.

Image segmentation is a procedure to separate structures of interest in images from background or other neighboring structures. It is a necessary prerequisite step for many medical imaging applications in radiology and radiation therapy. These applications may include automatic organ delineation, quantitative tissue classification, surface extraction, visualization and image registration, etc (Pham *et al.*, 2000; Suri *et al.*, 2002). For instance, Pham and coworkers divided segmentation algorithms into eight categories: thresholding, region growing, classifiers, clustering, Markov random field models, artificial neural networks, deformable models and atlas-guided approaches.

There are several commercial and academic software tools that support different segmentation algorithms. In general, commercial software packages have better implementations with a user-friendly interface for manual and semi-automatic segmentation methods, but often lag behind the latest development in the field. In contrast, academic software packages, such as ITK (Yoo *et al.*, 2002), BioImage Suite (Papademetris *et al.*, 2005), MIPAV (McAuliffe *et al.*, 2001), and ImageJ (Abramoff *et al.*, 2004), may tend to be oriented towards single-modality applications and less friendly in handling multimodality images as proposed here.

Most automatic algorithms attempt to utilize image intensity variations or image gradient information. However, for low contrast images, many of these algorithms tend to provide suboptimal solutions that are not clinically acceptable. For such cases, it has been demonstrated that if multiple images are available for the same object (same image modality or different image modalities), all the available complementary information can be fed into the segmentation algorithms to define so called biophysical target (El Naqa *et al.*, 2007). Thus, the segmentation algorithms would benefit from the complementary information from different images and consequently the accuracy of the final segmentation results could be improved. Similar approaches have been applied for detecting blood-wall interface of heart ventricles from CT, MRI and ultrasound images using a snake deformable model (Sebbahi *et al.*, 1997), for classifying coronary artery plaque composition from multiple contrast MR images using K-means clustering algorithm (Zheng *et al.*, 2005), and for defining tumor target volumes using PET/CT/MR images for radiotherapy treatment planning by using a multi-valued deformable level set approach as in our previous work. Mathematically, such an approach is a framework that could be thought of as a mapping from the imaging space to the ‘perception’ space as identified by the radiologists (El Naqa *et al.*, 2007):

$$\text{Biophysical target} = f(CT, PET, MRI, \dots; \lambda) \quad (1)$$

where $f(\cdot)$ is the mapping function from the different imaging modalities to the target space parameterized by λ , which represents users’ defined set of parameters representing the prior knowledge.

Despite the opportunities presented by this framework for streamlining integration of multiple imaging modalities for better tissue classification or target definition, there are several challenges that should be addressed before clinical implementation could be achieved. First, image misalignment is an issue when dealing with images acquired from different scanners. This is partially resolved for PET/CT but not for many other image modalities. Therefore, methods for image registration should be incorporated into the framework. The second and more challenging issue in our view is the characterization of the mapping in equation 1 because it relies on human higher-level expertise to be translated into cues that computer algorithms can understand. These challenges have motivated us to develop a software tool to support such a multimodality image segmentation framework and potentially for learning information from user’s interactions. To our best knowledge, the MIASYS software is the first tool to offer a dedicated and comprehensive framework to cope with this current emerging need in therapeutic and diagnostic radiological applications.

2. SEGMENTATION ALGORITHMS

Most existing segmentation algorithms are dedicated for single modality image analysis, which is by itself a daunting task. A few of these algorithms, to be presented in the following, could be extended to support simultaneous

segmentation of multiple images in the proposed multimodality image segmentation framework. These are reviewed in more details for completeness.

2.1 Multiple image thresholding

Thresholding is one of the most basic image segmentation methods. Thresholding methods are commonly used for delineating objects with high contrast with respect to the surrounding image background. Threshold values could be selected experimentally. For example, in detecting tumors in PET based on cutoff values of the standardized uptake value (SUV), a threshold value is usually selected as $SUV > 2.5$ or 40% of maximum SUV (Nestle *et al.*, 2005). In another example, an optimal threshold image intensity value was selected iteratively to separate the lungs from the body and chest wall structures (Hu *et al.*, 2001).

In this work, we expanded the thresholding method to support multiple images in the way that different threshold values could be applied to the different images and the thresholding results for different images are combined in logical ways to form the final result. We use the *thresholding conditions* notion to describe such multiple image thresholding operations. For example, a *thresholding condition* could be “ $Im1 < 100 \ \& \ Im2 > 50 \ | \ 20 < Im3 < 150$ ”, where $Im1$, $Im2$ and $Im3$ denote the intensity values of images 1, 2 and 3. Our software tool (to be discussed later) is able to interpret the meaning of such a *thresholding condition* expression and carries out all the mathematical and logical computations to yield the final combined result. In fact, the software tool is implemented with MATLAB and it accepts any valid MATLAB expression as a *thresholding condition*. The expressions could contain any arithmetic, logical operators and parentheses. The new thresholding method, which takes such mathematic expressions, is flexible, easy to use and very powerful.

2.2 Clustering algorithms

Clustering algorithms are frequently used for different image analysis problems such as image segmentation, object recognition, and image retrieval (Jain *et al.*, 1999). For image segmentation, they are used to automatically discriminate different tissue types based on primitive image features such as image intensity. One of the most commonly used algorithms is the K-means algorithm. Another algorithm that we have found to be more robust is the fuzzy C-means (FCM) algorithm. Both algorithms are discussed below.

Fuzzy C-means algorithm

Similar to other clustering algorithms, the goal of the fuzzy C-means (FCM) algorithm (James, 1981) is to divide the image histogram into a few clusters and to iteratively find the center of each cluster by minimizing the following system energy function:

$$J(x, c) = \sum_{i=1}^N \sum_{k=1}^K \|x_i - c_k\|^2 \quad (2)$$

where x_i is the image intensity for pixel i , N is the total number of pixels in the image, K is the total number of clusters, and c_k is the cluster center intensity value for cluster k .

In the FCM algorithm, a fuzzy membership function is defined and computed as equation 3, and the cluster center c_k^n is updated according to equation 4.

$$u_{ik}^n = \frac{\|x_i - c_k^n\|^{-2}}{\sum_{k=1}^K \|x_i - c_k^n\|^{-2}} \quad (3)$$

$$\mathbf{c}_k^{n+1} = \frac{\sum_{i=1}^N (\mathbf{u}_{ik}^n)^b \mathbf{x}_i}{\sum_{i=1}^N (\mathbf{u}_{ik}^n)^b} \quad (4)$$

where \mathbf{u}_{ik}^n is the fuzzy membership probability that image pixel \mathbf{x}_i belongs to cluster k at iteration n , and \mathbf{c}_k^n is the updated cluster center intensity value for cluster k at iteration n , b is a user defined parameter and $0 < b < 1$.

The user starts FCM method by setting the value of K , then the \mathbf{c}_k^0 can be automatically and randomly initialized, and the iterations are repeated by computing equations 3 and 4 alternatively. The iterations stop when \mathbf{c}_k^n is stabilized.

Extension fuzzy C-means algorithm to multiple images

The FCM method can be naturally expanded to support multiple images by defining \mathbf{x}_i and \mathbf{c}_k^n as vectors instead of scalar values:

$$\mathbf{x}_i = \langle x_{i,1}, x_{i,2}, \dots, x_{i,M} \rangle \quad (5)$$

$$\mathbf{c}_k^n = \langle c_{k,1}^n, c_{k,2}^n, \dots, c_{k,M}^n \rangle \quad (6)$$

where M is the total number of images in the multimodality image data set, $x_{i,m}$ is the image pixel intensity value for the pixel i in the image m ($1 < m < M$), $\mathbf{c}_{k,m}^n$ is the cluster center intensity value for the cluster k in the image m for iteration n . With \mathbf{x}_i and \mathbf{c}_k^n defined as vectors, equations 3 and 4 can be rewritten as:

$$\mathbf{u}_{ik}^n = \frac{\left(\sum_{m=1}^M \alpha_m (x_{i,m} - c_{k,m}^n)^2 \right)^{-2}}{\sum_{k=1}^K \left(\sum_{m=1}^M \alpha_m (x_{i,m} - c_{k,m}^n)^2 \right)^{-2}} \quad (7)$$

$$\mathbf{c}_{k,m}^{n+1} = \frac{\sum_{i=1}^N (\mathbf{u}_{ik}^n)^b \mathbf{x}_{i,m}}{\sum_{i=1}^N (\mathbf{u}_{ik}^n)^b}, m = 1, M \quad (8)$$

where α_m is the user defined weighting parameter for image m .

In this case, the computation of the fuzzy membership value \mathbf{u}_{ik}^n is contributed by all the images in the multimodality image dataset. The new weighting parameters α_m control the contribution from the different images according to the users' prior knowledge.

The FCM algorithm works on the image intensity histogram domain. Image pixel spatial information is not considered in the algorithm. There is also no difference in applying this algorithm to 2D images or to 3D volume images. Better FCM algorithms that consider image pixel spatial information, which we would like to include into the software tool in the future, have been reported in the literature (Pham, 2001; Weiling *et al.*, 2007).

K-means clustering algorithm

The K-means algorithm (Anderberg, 1973) is actually a precursor of the FCM algorithm. It uses hard membership function instead of the fuzzy membership function. Performance of K-means algorithm is in general comparable but typically less than the performance of the FCM algorithm. We have also implemented K-means algorithm as an alternative of FCM algorithm because it is commonly used in many applications. However, both K-means and FCM

algorithms may in general suffer from lacking a proper spatial neighborhood definition, which is addressed in the active contour algorithms discussed next.

2.3 Active contour algorithms

Deformable models are geometric representations for curves (in 2D) or surfaces (in 3D) that are defined explicitly or implicitly in the imaging domain. These models deform under the influence of force-like equations which are computed from the image data (Sethian, 1999; Xu *et al.*, 2002). The idea is that contours of structures in the images are characterized by sharp variations in the image intensity, and therefore the deformable models can be warped to match the contours by means of energy minimization (Xu *et al.*, 2002; Aubert, 2006; Osher and Fedkiw, 2003).

So-called ‘snakes’ algorithms were among the first deformable models developed (Kass *et al.*, 1988). Snakes use an explicit parametric representation of the object boundary that deforms by means of energy minimization (or dynamic force equilibrium). Mathematically, if the deformable model is represented by:

$$C(s) = \{x(s), y(s), z(s)\}, s \in [0, 1] \tag{9}$$

Then, its movement is governed by the following functional:

$$J(C(t)) = \int_0^1 \left(\alpha(s) \left| \frac{\partial C(s,t)}{\partial s} \right|^2 + \beta(s) \left| \frac{\partial^2 C(s,t)}{\partial s^2} \right|^2 \right) ds + \gamma \int_0^1 P(C(s,t)) ds \tag{10}$$

where the first term corresponds to internal energy and controls the tension and rigidity of the model. The second term corresponds to external energy, where P represents the potential energy, which could be given as $g(|\nabla I|)$, and g is selected to be a monotonically decreasing function of the gradient of image intensity I . Other examples could include using pressure or balloon representations for representing an expanding object or other diffusing functions. Using calculus of variation techniques, the solution to equation 10 is obtained by solving the associated Euler-Lagrange PDE (Osher and Fedkiw, 2003; Xu *et al.*, 2002):

$$\frac{\partial}{\partial s} \left(\alpha \frac{\partial C}{\partial s} \right) + \frac{\partial^2}{\partial s^2} \left(\beta \frac{\partial^2 C}{\partial s^2} \right) + \nabla P(C(s,t)) = 0 \tag{11}$$

However, the formulation in equation 11 is non-convex and suffers from several drawbacks such as sensitivity to contour initialization, a dependency on parameterization, and an inability to account for topological adaptation (e.g., delineation of a necrotic tumor). To solve the sensitivity problem, the geodesic active contour model was proposed (Caselles *et al.*, 1997) which in principle is equivalent to equation 10 if the smoothness constraint is eliminated (i.e., by setting $\beta = 0$). This has led to the development of flow or curve evolution concept:

$$\frac{\partial C}{\partial t} = \vec{V}(\kappa) \tag{12}$$

where \vec{V} is the velocity function (of magnitude V) in the normal direction (\vec{N}), and κ is the local contour curvature. However, to resolve the main problem of parameterization and topological adaptation, the level set approach was proposed. (Sethian, 1999)

In the level set approach, the curve (in equation 12) is embedded in an implicit level set function ϕ . This function defines sets of contour values and positions, including the target boundary at the zero level ($\phi(C) = 0$). In this case, we choose to rewrite the evolution equation as:

$$\frac{\partial \phi}{\partial t} = V(\kappa) |\nabla \phi| + F(\Theta) \tag{13}$$

where V is defined to be proportional to the curvature and inversely proportional to the image gradient; and $F(\Theta)$ is the external force constraint with vector parameter Θ that could be used to add context-knowledge information such as

shape priors. The level set function (ϕ) is typically selected as a signed distance function. Efficient solutions were developed for equation 13 by using finite difference and fast marching methods (Sethian, 1999).

2.3.1. "Active-contour-without-edge" algorithm

"Active-contour-without-edge" algorithm is one of the frequently used active contour image segmentation algorithms, originally reported by Vese and Chan (Chan and Vese, 2001). Unlike many other algorithms, it is based on regional average intensity value instead of image gradient since image gradients tend to be more sensitive to noise and therefore less reliable.

The original algorithm

To separate an image into two mutually exclusive partitions, the following system energy equation is to be minimized:

$$F(c_1, c_2, C) = \int_{\Omega_1} (I - c_1)^2 d\Omega + \int_{\Omega_2} (I - c_2)^2 d\Omega + \mu|C| + \nu \cdot \Gamma(C) \quad (14)$$

where I is the image intensity, Ω_1 and Ω_2 are the two partitions, Ω_1 is inside the contour defined by the level set and Ω_2 is outside the contour, c_1 and c_2 are the average image intensity in partition Ω_1 and Ω_2 respectively, C is the partition boundary, and $|C|$ is the total length of C for 2D images or total surface area of C for 3D images, ν and μ are user selected weighting constants. $\Gamma(C)$ is the area inside C for 2D images or the volume inside C for 3D images.

The level set formation for equation 14 is

$$F(c_1, c_2, C) = \int_{\Omega} \left((I - c_1)^2 H(\phi) + (I - c_2)^2 (1 - H(\phi)) + \mu \cdot \delta(\phi) |\nabla \phi| + \nu \cdot H(\phi) \right) d\Omega \quad (15)$$

where $\Omega = \Omega_1 + \Omega_2$ is the entire image, H is the Heaviside function (a unit step function) of level set ϕ , and δ is the delta function of ϕ .

The iterative solution for the level set equation is given by:

$$\frac{\partial \phi}{\partial t} = \delta_{\epsilon}(\phi) \left(\mu \operatorname{div} \left(\frac{\nabla \phi}{|\nabla \phi|} \right) - \nu - (I - c_1)^2 + (I - c_2)^2 \right) \quad (16)$$

where $\delta_{\epsilon}(\phi)$ is delta function of level set ϕ with width ϵ . Note that the constant parameter ν is also often known as the balloon force as it controls the constant inflation or deflation of the level set.

The two average image intensity values c_1 and c_2 are updated per iteration according to:

$$c_1(\phi) = \frac{\int_{\Omega} I \cdot H(\phi) d\Omega}{\int_{\Omega} H(\phi) d\Omega} \quad (17)$$

$$c_2(\phi) = \frac{\int_{\Omega} I(1 - H(\phi)) d\Omega}{\int_{\Omega} (1 - H(\phi)) d\Omega} \quad (18)$$

In our implementation, we have also added an additional spring force $(c_1 - c_2)^2$ to further balance the distance between c_1 and c_2 . The level set equation in our implementation is given by:

$$\frac{\partial \phi}{\partial t} = \delta_{\epsilon}(\phi) \left(\mu \operatorname{div} \left(\frac{\nabla \phi}{|\nabla \phi|} \right) - \nu - \lambda_1 (I - c_1)^2 + \lambda_2 (I - c_2)^2 + \lambda_3 (c_1 - c_2)^2 \right) \quad (19)$$

where λ_1 , λ_2 and λ_3 are user configurable constant parameters that were omitted previously for simplicity.

Extension to multiple images

We used the concept of multi-valued level set to extend the “active-contour-without-edge” method to multiple images originally suggested for processing multi-channelled color images as follows (Chan *et al.*, 2000; Shah, 1996):

$$\frac{\partial \phi}{\partial t} = \delta_{\epsilon}(\phi) \left(\mu \operatorname{div} \left(\frac{\nabla \phi}{|\nabla \phi|} \right) - \nu - \sum_{m=1}^M \alpha_m \left(\lambda_1 (I_m - c_{1,m})^2 - \lambda_2 (I_m - c_{2,m})^2 - \lambda_3 (c_{1,m} - c_{2,m})^2 \right) \right) \quad (20)$$

Where α_m is user defined relative weighting parameters for image m with image intensity u_m , M is the total number of images, $c_{1,m}$ and $c_{2,m}$ are the c_1 and c_2 values for image m , they are computed using I_m as intensity I in equations 17 and 18. In this generalization, the level set iterative evolution is contributed by all the images in the multimodality image dataset. The weighting parameters α_m control the amounts of contribution from different images according to the user’s perception of importance.

3. MIASYS SOFTWARE TOOL

We have developed a software tool in order to demonstrate the new multimodality segmentation framework. The software tool provides a platform for user interaction and evaluation of different segmentation methods. The software tool is denoted as “MIASYS” for Multimodality Image Analysis System. It is programmed with MATLAB 7.0, compatible with any computer platform that is supported by MATLAB. Figure 1 and Figure 2 show screenshots of the MIASYS software tool GUI (graphical user interface) and illustrate many of the important features that are available within the software.

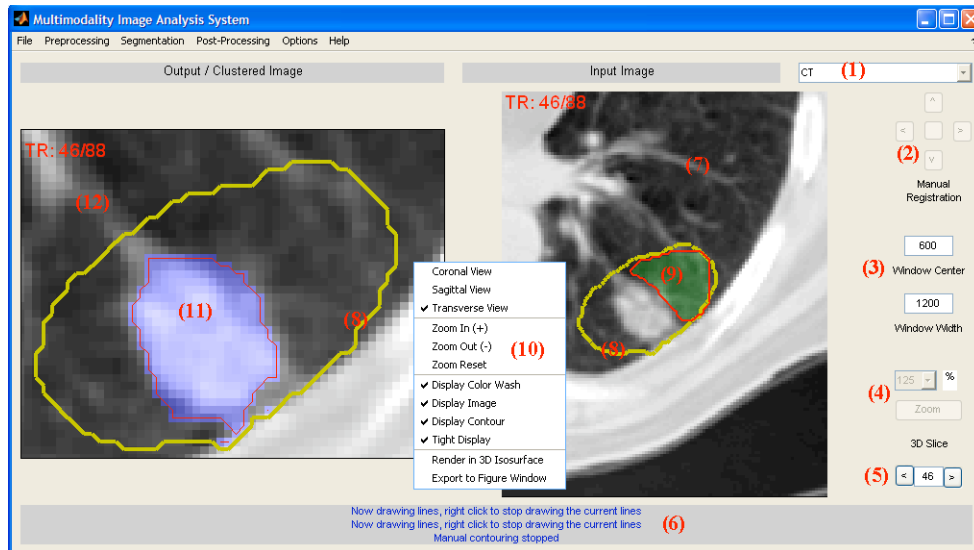


Figure 1. Screen shot of the MIASYS software tool. (1) image selector, (2) manual registration, (3) window level settings, (4) zoom control, (5) 3D slice number control, (6) status information, (7) the working image panel, (8) ROI contour, (9) temporary segmentation result, (10) right mouse click context menu, (11) segmented regions, and (12) segmentation result display panel, zoomed in to ROI.

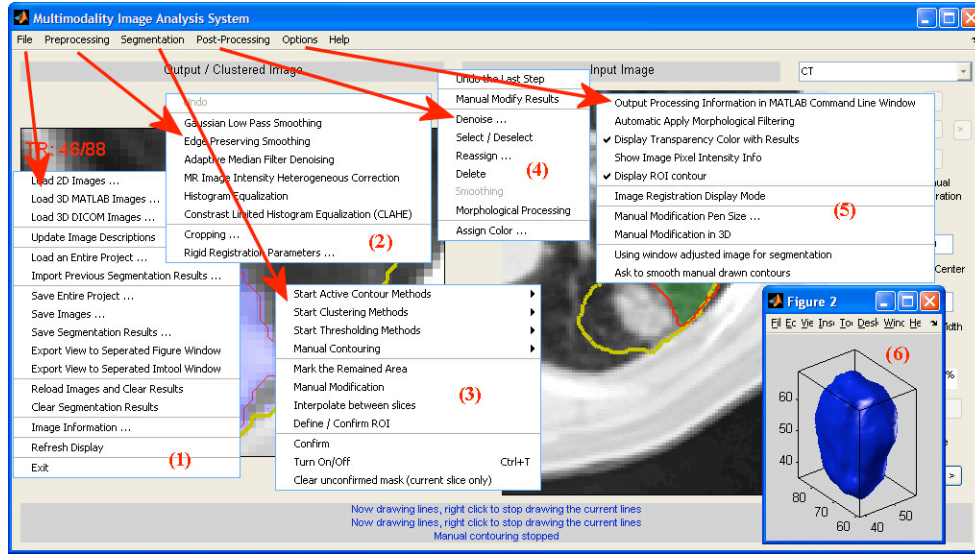


Figure 2. GUI menus and a separate 3D viewing panel showing many of the features included with the MIASYS software. (1) File menu, (2) preprocessing menu, (3) segmentation menu, (4) post-processing menu, (5) options menu, and (6) 3D isosurface rendering panel.

3.1 Overview

Figure 3 shows the basic steps of using the MIASYS software tool to perform image segmentation. After a set of images is imported, rigid image registration is applied to align all images. Image preprocessing procedures, such as cropping, zooming, re-sampling, smoothing and contrast enhancement, can be selectively applied in order to improve the performance for both automated and manual segmentation methods. MIASYS provides an easy and interactive way for the user to manually define ROIs (region of interest) which defines the actual computation region (instead of using the entire image for computation) and therefore helps to improve the computation speed and the overall performance of the system. The user can select different segmentation methods to sequentially segment the images into multiple partitions. After all the target partitions are defined, users are allowed to manually modify the overall segmentation results in post-processing steps. Furthermore, the software provides metrics for quantitative analysis of the segmentation results and ability to export these results into external files for further use.

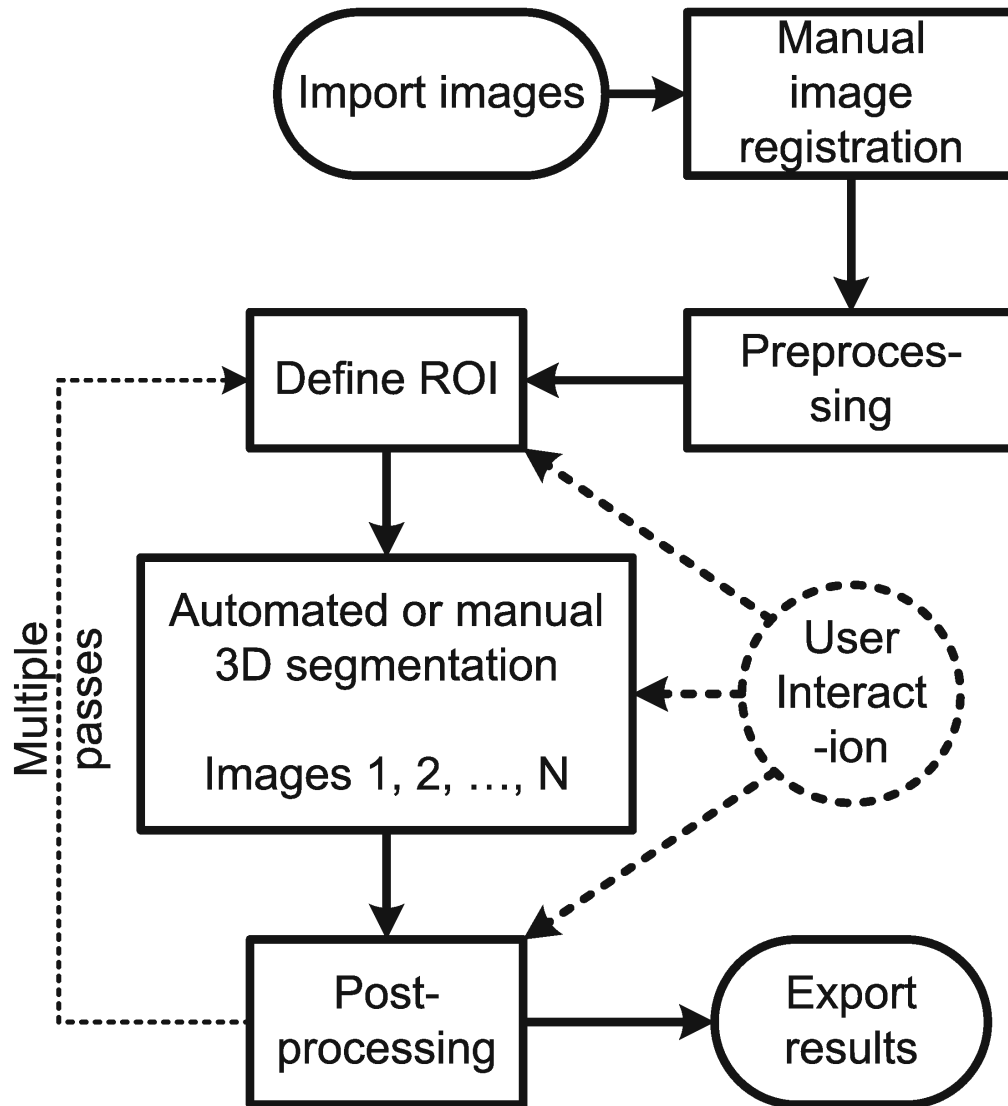


Figure 3. The main workflow. Note that the actual segmentation step could be done in multiple passes. Each pass will define one or more image segments. Different segmentation methods could be applied in the different passes as desired.

3.2 Data import

MIASYS is capable of importing DICOM and many other image file formats as well as MATLAB native data files. There are differences between 2D and 3D image formats because not all image file formats support 3D. For 2D, the supported file formats include DICOM, IMA, MATLAB and any other regular image file formats like PNG, JPG, TIFF, etc. For 3D datasets, the software tool currently only supports DICOM and MATLAB files. Spatial information, like pixel spacing and slice thickness are automatically read from the DICOM files. Other unsupported images can be loaded into MATLAB outside the software tool using MATLAB built-in functions or user defined functions for other imaging platforms such as Interfile or Analyze. In any case, if pixel spacing information for instance is not available from the image file, the user will be prompted to enter the information manually.

3.3 Image registration

Images of different modalities are often acquired from different scanners at different times. Such images are often not only misaligned, but could also have different voxel dimensions, different image dimensions (number of voxels in each 3D direction). Therefore, image registration is a necessary step to ensure that the multiple images are properly aligned before the segmentation procedures are applied. MIASYS currently supports some basic automatic and manual rigid registration methods. The first image is by default selected as the reference image (the fixed image). All other images are registered separately to the reference image.

3.3.1 Automatic rigid registration

ITK image registration algorithms has been previously implemented and bridged, programmed in C and C++, to MATLAB (Wu *et al.*, 2007). We have integrated this work into MIASYS. We currently have only included one method - affine rigid registration using mutual information metric, similarity 3D transform and gradient descent optimizer (Ibanez *et al.*, 2005). In this method, mutual information computation is based on Mattes' method (Mattes *et al.*, 2003).

3.3.2 Manual registration

MIASYS also supports translation only manual registration. The panel of directional buttons marked as (2) in **Figure 1** are the GUI controls to shift the image with respect to the reference image. For 3D images, the image shifting direction is consistent with the current image display orientation.

As mentioned earlier, all other images are registered with respect to the reference image. There is an internal transformation matrix associated with every image. Users can manually edit any of these transformation matrices to achieve any type of affine transformations. If necessary, users could also use other available image registration tools, such as MIPAV (McAuliffe *et al.*, 2001), to perform registration and then insert the resultant transformation matrix into MIASYS. We also plan to include multimodality deformable registration algorithms (Hermosillo *et al.*, 2002) as part of the software in future work.

3.4 Image preprocessing tools

3.4.1 Geometrical processing

Resampling, 3D cropping and 3D zooming functions are implemented for geometrical manipulation of the images. The cropping feature helps to reduce the image dimension and therefore to save subsequent computation time. The zooming feature helps to set the center of the image to a desired magnification level and to resample the images to different voxel resolutions.

3.4.2 Image intensity processing

Image intensity preprocessing steps are important, especially for image intensity based algorithms. Available preprocessing filters in MIASYS include a Gaussian low pass smoothing filter, edge preserving smoothing filter (Tomasi and Manduchi, 1998), adaptive median denoising filter (Nieminen *et al.*, 1987), histogram equalization filter, contrast limited histogram equalization (CLAHE) filter (Zuiderveld, 1994), and a MR image intensity heterogeneity correction filter (Salvado *et al.*, 2006).

3.5 Multiple pass multiple modality 3D segmentation

Our strategy for image segmentation with MIASYS is to sequentially segment the images into different partitions, one by one. Already segmented image regions will be excluded from any subsequent segmentation processing. User interaction is an important part of the software design. In many cases, users may find that manual intervention using manual editing tools (to be discussed next) may provide help for subsequent auto-segmentation application.

3.5.1 Manual contouring

Manual contouring remains very important in any image segmentation software because automatic segmentation algorithms may often fail to generate acceptable results in many situations. In MIASYS, manual contouring is also used to define the ROI, and to initialize the active contour algorithm. Manual contouring is used as a learning tool for multimodality segmentation researchers to record and better understand experts' knowledge.

Three manual segmentation methods

MIASYS supports three basic manual contouring methods: continuous manual contouring, line segment manual contouring and manual painting. Examples of these methods are shown in Figure 4. Manually drawn contours could be further smoothed by MIASYS. For 3D image, manual contours on discontinuous slices could be interpolated to generate the contours for the slices in between.

Manual contouring on multiple images

MIASYS can display two to three images simultaneously in different color channels. Originally designed for overlaying images for registration evaluation, this feature is useful in manual contouring because it allows the users to see more than one image simultaneously and to better distinguish the structure boundaries from multiple images.

3.5.2 Automatic segmentation

When an automatic segmentation algorithm is used at a certain step, the results of the algorithm will be displayed as a temporary contour. Users can either confirm the result or to discard it. In such a way, users have the option to try different algorithms or different parameters of the same algorithms.

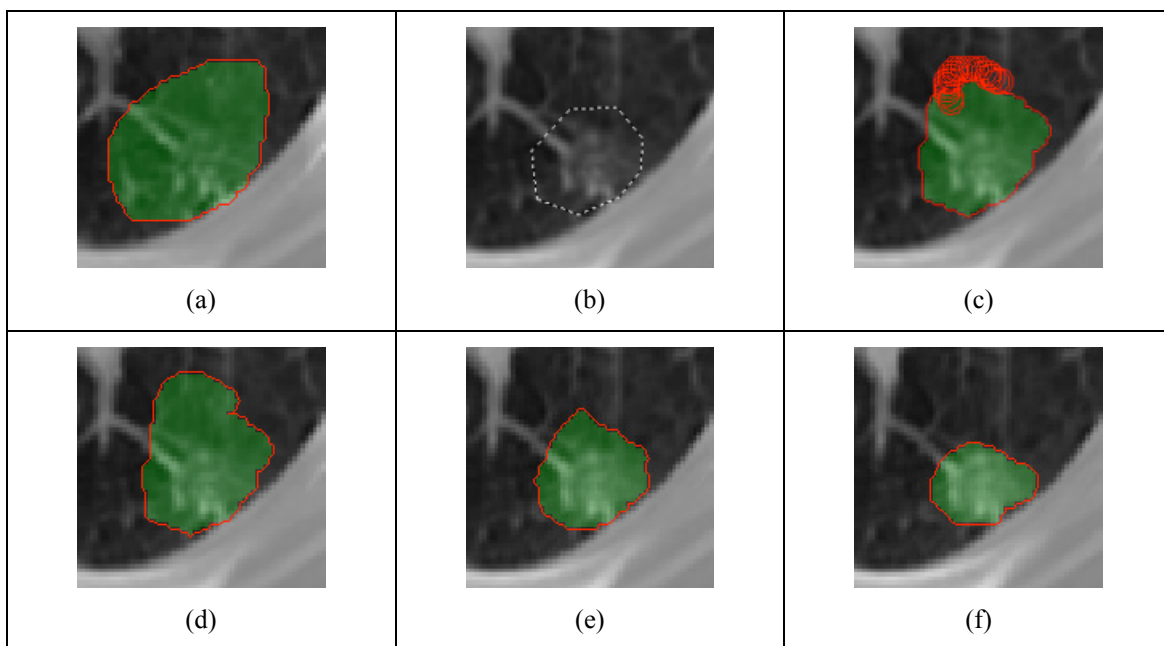


Figure 4. Examples of different manual contouring methods. (a) Continuous drawing, (b) line segments drawing, (c) manual painting in progress, (d), (e) and (f) contour interpolation between slices where (e) is the interpolation between (d) and (f).

3.6 Post-Processing

MIASYS is equipped with functions for refinement of segmentation results. These functions include: 1) deleting a segmented region; 2) combing all small regions (region size smaller than a certain user set threshold value) into their neighbor regions. This is especially useful for results generated by fuzzy clustering methods; 3) selecting a segmented region and reassigning the region number; 4) smoothing a segmented region by using active contour deformation model (minimizing contour curvature); 5) morphologic filtering on the segmented regions to smooth the boundaries; 6) manual painting. Figure 5 shows examples of using different post-processing operations on segmentation results obtained by FCM clustering method. Spatial boundary discontinuity, which is often seen as small isolated patches in the segmentation results, is typically an issue in clustering algorithms like FCM. This example demonstrates the possibility to use different post-processing operations to achieve satisfactory results.

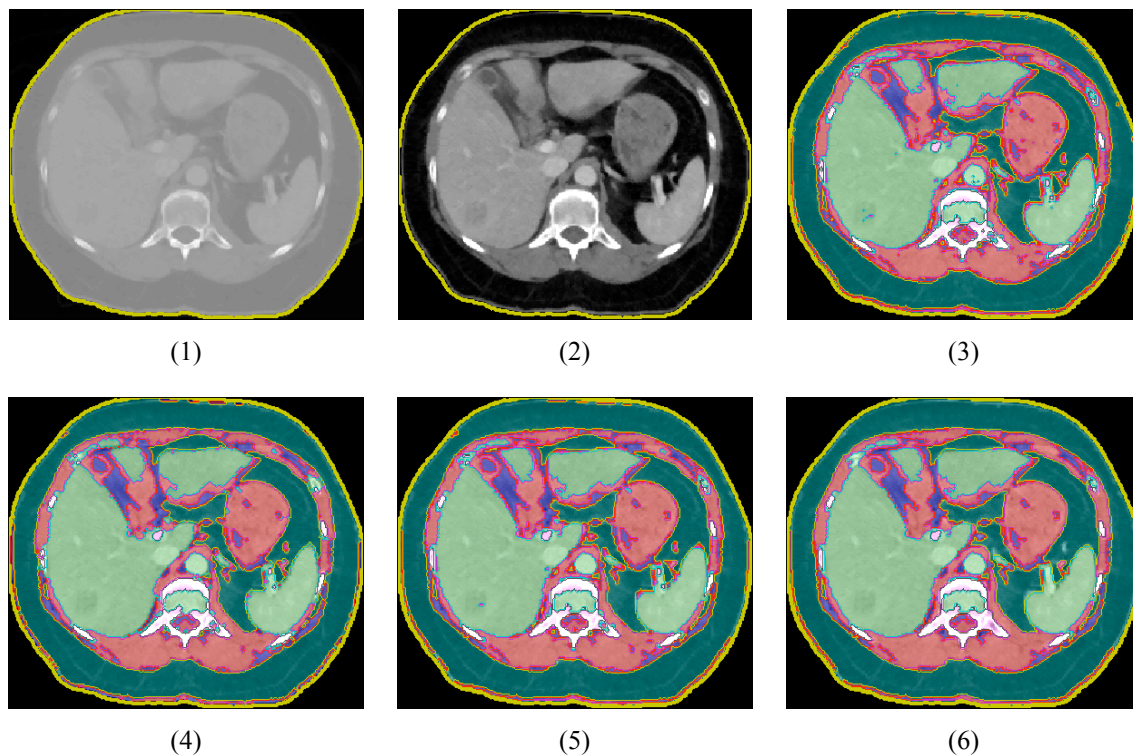


Figure 5. A demonstration of using fuzzy C-mean (FCM) clustering algorithm and post-processing operations. (1) the CT image, (2) the window level-adjusted CT image, (3) the initial result by FCM, (4) the result after applying morphological smoothing with disk size = 1 pixel, (5) the result after using denoising to remove small patches of size ≤ 5 pixels, and (6) the result after using denoising filter to remove small patches of size ≤ 21 pixels.

3.7 Exporting segmentation results and quantitative analysis

MIASYS can provide statistical information for each image partition. Such information along with the user's segmentation parameters could be saved into computer files for further reference. MIASYS can also export the segmentation results as contour point coordinate values. Such contour point coordinates could be further converted into DICOM format outside the MIASYS tool and loaded into a treatment planning system for radiation therapy applications.

3.8. Additional important features in MIASYS

The MIASYS tool has many other useful features to facilitate better image segmentation tasks. The followings are a few important ones.

Using ROI to speed up computation: users can promptly define and redefine ROI using provided manual contouring tools and the contour interpolation feature. The software tool uses the ROI information to speed up the computation for the automatic segmentation algorithms by restricting the computation within the ROI region.

File and project functions: users can save the complete working status, including all images, settings and current segmentation results, into a project file. The saved project file can then be loaded in a later session so that the previous unfinished work can be continued.

Undo: both the last preprocessing and post-processing step can be undone, for the last step only. This gives the user a second chance if this last step did not provide expected results.

3D visualization: MIASYS supports simple 3D image viewing. Users can select the slice number to view, and can view in superior-inferior, lateral, or anterior-posterior directions. The software can also render the segmentation results as 3D object using the 3D isosurface technique available with MATLAB.

Window level adjustment: image window level can be adjusted for display purposes. The window level setting can also be used to transform the image intensity. Segmentation results by automatic segmentation algorithms may be improved by using these contrast enhanced images.

4. EXAMPLE APPLICATIONS AND RESULTS

There are many radiology and radiation therapy applications that would benefit from the proposed multimodality image segmentation framework. For demonstrative purposes, we will present two representative examples. The first example is a case of delineation of the lung tumor using PET and CT images for radiation treatment planning purposes. The second example is a case of tissue classification of coronary artery plaque from multiple contrast MRI images in diagnosis or prognosis of heart disease risk in cardiovascular radiology. The segmentation results were analyzed qualitatively and quantitatively.

The quantitative analysis relied on comparing the automatic segmentation results with the experts' manually drawn contours using the Dice similarity metric (*DSC*) (Dice, 1945):

$$DSC = 2 \times \frac{V_M \cap V_A}{V_M + V_A} \quad (21)$$

where V_M is the area inside the manually drawn contour for the object, V_A is the area inside the automatic segmented object, \cap is the joint operator. The values of *DSC* are between 0 and 1, stands for the matching between the two contours. $DSC = 0$ means no overlapping at all, and $DSC = 1$ means perfect matching.

4.1. Lung tumor delineation with CT and PET images for radiotherapy treatment planning

In radiation therapy treatment planning of lung cancer, CT and PET images are often registered and fused together to help the physician to more accurately delineate the 'true' tumor volume. CT images contribute to determine the anatomic boundaries while PET images contribute to determine the tumor metabolic activity boundary (Beyer *et al.*, 2000; Bradley *et al.*, 2004a; Hanley *et al.*, 1999; Zangheri *et al.*, 2004). We have successfully applied the MIASYS software tool for tumor delineation using such co-registered CT and PET images.

Figure 6 Figure 6 shows a pair of co-registered CT and PET images of a lung tumor. The tumor is indicated by arrows. The CT and PET images were used in the following examples.

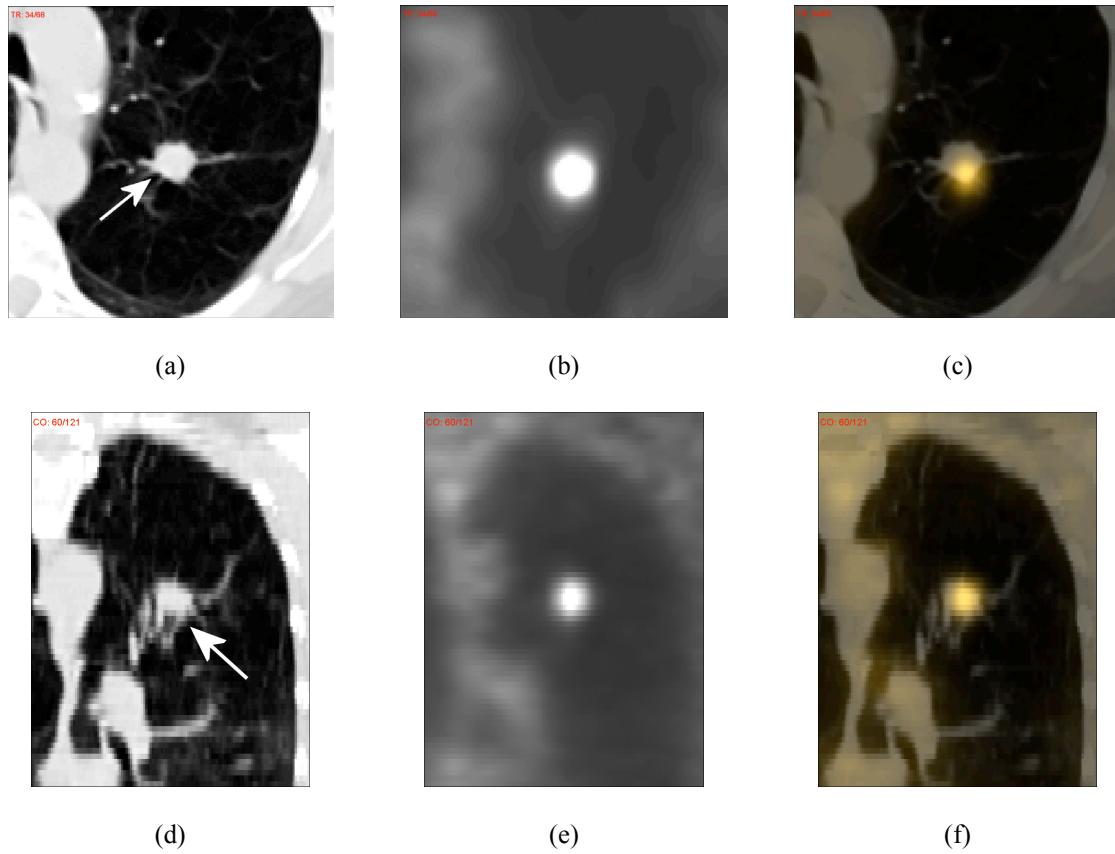


Figure 6. Co-registered CT and PET images of a lung cancer tumor. The tumor is indicated by the arrows. (a), (b) and (c) are the transverse views, and (d), (e) and (f) are the coronal views, (a) and (d) are CT images, (b) and (e) are PET images, (c) and (f) are fused CT and PET images.

Figure 7 shows the results of the generalized “active-contour-without-edges” algorithm and the qualitative comparison to the manually defined tumor boundaries. The GTV structure (the yellow contour) was drawn on CT by a radiation oncologist (A. N.), and the MTV structure (the red contour) was drawn on PET. It can be seen that the automatic segmentation contour (the green contour) encloses the tumor on the PET/CT fused image very well since both CT and PET information were incorporated in the segmentation computation. This resulted in improved agreement relative to discrepancy in the blinded manual contouring of PET and CT images as summarized in Table 1.

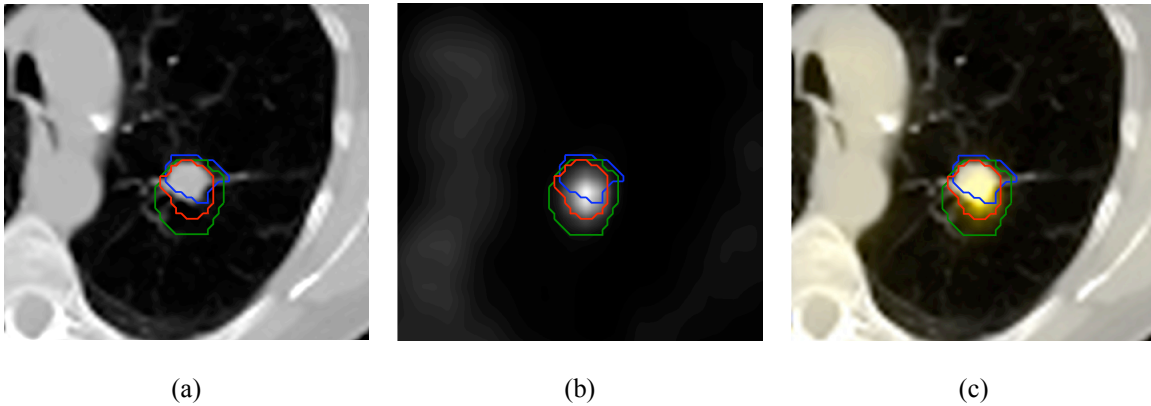


Figure 7. Results of using an active contour algorithm to segment the lung tumor with co-registered CT and PET images. (a) is CT, (b) is PET, and (c) is the fused CT and PET. The blue contour is the GTV contour manually drawn on CT by radiation oncologist. The green contour is the MTV contour manually drawn on PET image by the physician. The red contour is the result of applying the active contour algorithm, which constitutes a compromise between the two contours in this case.

Table 1. Dice similarity metric between manual contours and automatic segmentation results in PET/CT lung cancer example.

	<i>Manual CT contour and Manual PET contour</i>	<i>Automatic contour and CT manual</i>	<i>Automatic contour and PET manual</i>
DSC	0.49	0.6	0.6

Figure 8 shows some demonstrative results obtained by using the generalized “active-contour-without-edge” algorithm, FCM clustering algorithm and thresholding algorithm. These example results demonstrate that different segmentation algorithms could be applied for the PET/CT images and would generate similar but slightly different results.

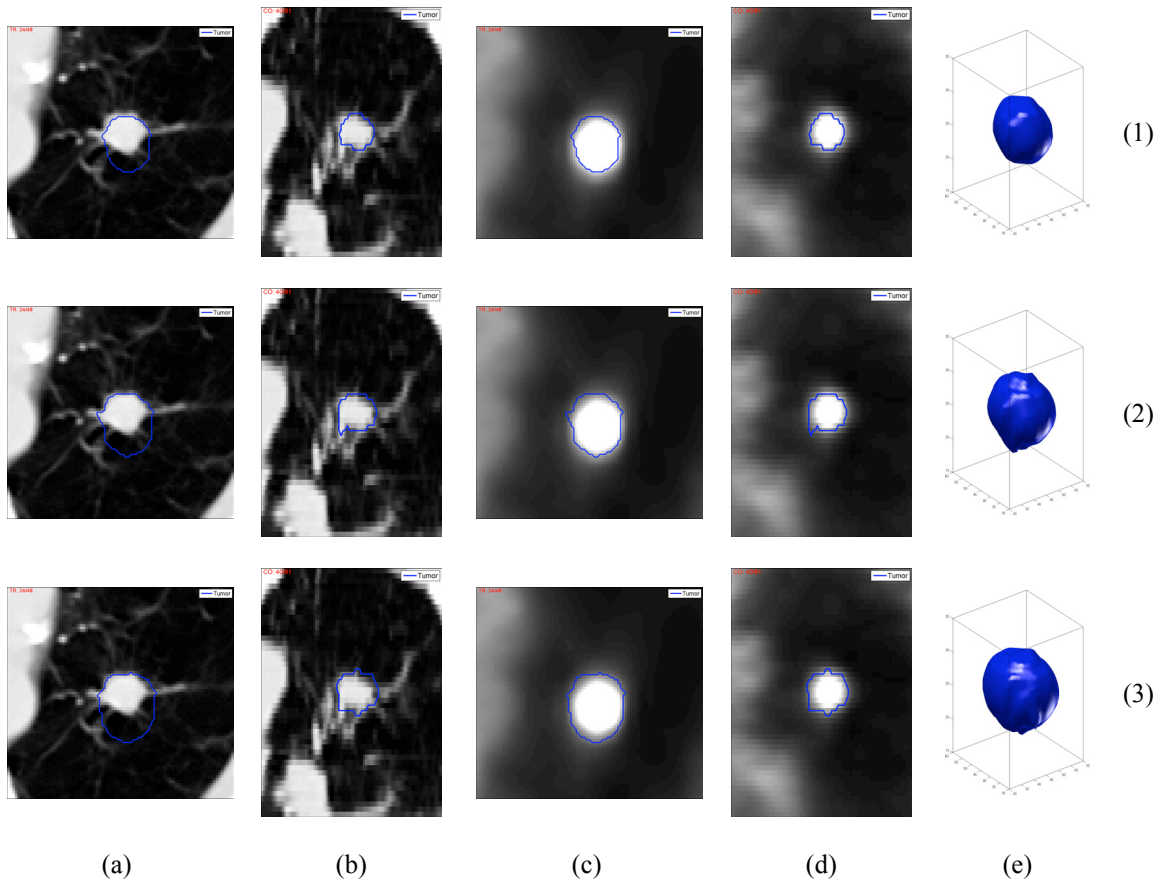


Figure 8. Examples of using the active contour algorithm, the FCM clustering algorithm and the thresholding method. Row 1 is the result by the active contour algorithm. Row 2 is the result of the FCM clustering algorithm. Row 3 is the result of the thresholding method with the condition “ $(CT > 500 \ \& \ PET > 1500) \ | \ (CT > 400 \ \& \ PET > 2000) \ | \ PET > 2500$ ”. Columns a, b, c, d and e are CT transverse, CT coronal, PET transverse, PET coronal view and 3D views, respectively. In this case, the methods yield similar results.

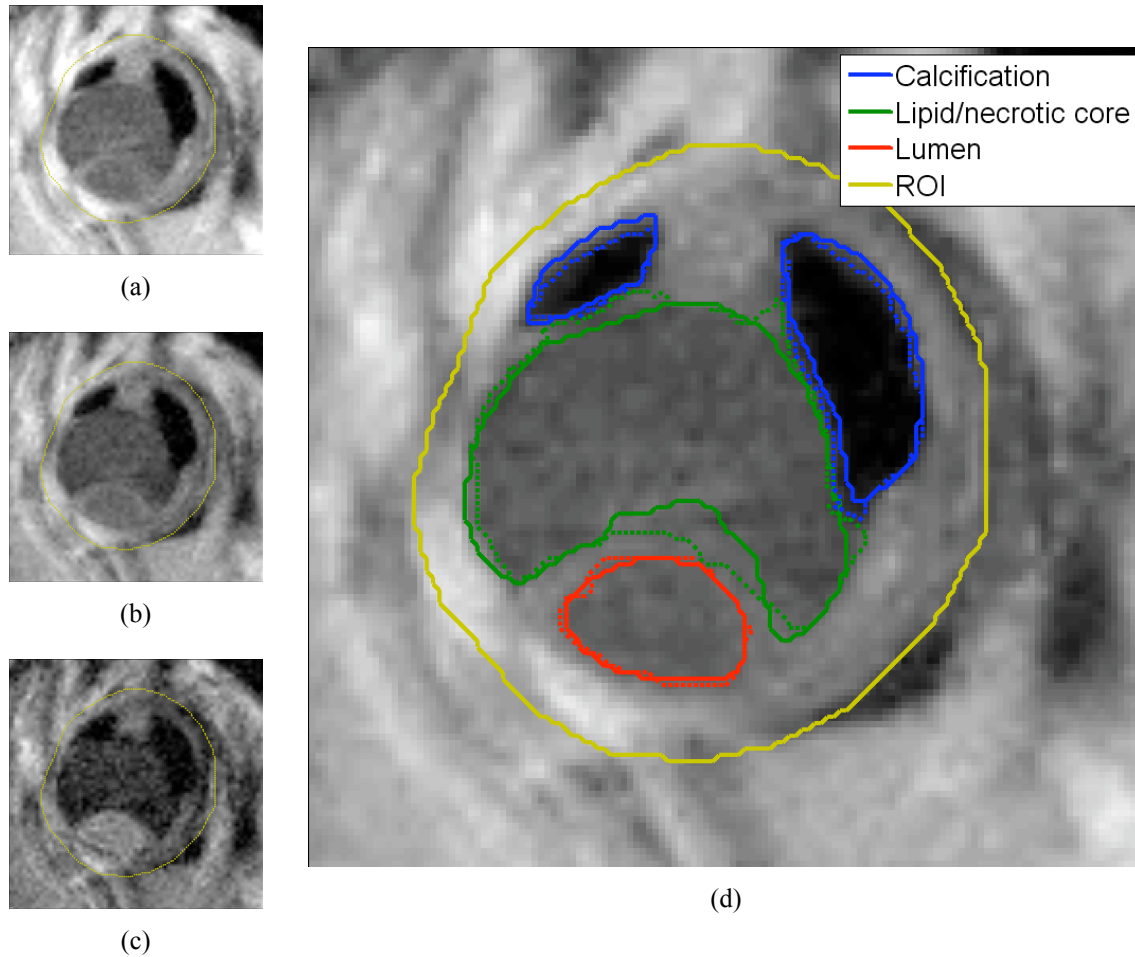


Figure 9. Examples of ex-vivo coronary artery plaque segmentation. (a) The PD slice, (b) the T1w slice, (c) the T2w slice, (d) the PD slice overlaid with both manual contours and automatically segmented contours for calcification, lipid components and artery lumen. The solid yellow lines are the manually drawn ROI region. The other solid lines are manually drawn contours. The dotted lines are the automatic segmentation results. The expert’s manual contour and the multimodality automated segmentation results are in good agreement.

4.2 Coronary artery plaque MR image analysis

The composition of an atherosclerotic plaque is an important predictor for thromboembolic events. Intraplaque hemorrhage and lipid core are considered especially high-risk components (Cappendijk *et al.*, 2005). Multi-contrast MR images can be applied for detection of these components. In this example, we used multiple MR images that have been acquired by scanning cadavers’ coronary artery tissue samples. The ex-vivo tissue samples were scanned using T1w (T1 weighting), T2w (T2 weighting) and PD (Proton Density) sequences. We used the generalized “active-contour-without-edges” algorithm to perform automatic image segmentation and compared the results to contours manually drawn by an experienced radiologist (J. Z.) for demonstration purposes. The artery lumen, the calcification component and the lipid core component were contoured as shown in Figure 9.

For the example shown in Figure 9, the computed Dice similarity metric values are summarized in Table 2. These values indicate that the automatic segmentation objects matched well with the expert’s contoured objects.

Table 2. Dice similarity metric between manual contours and automatic segmentation results in 4.2. Coronary artery plaque MR example.

	<i>Calcification</i>	<i>Lipid core</i>	<i>Lumen</i>
DSC	0.89	0.92	0.95

5. DISCUSSION

We have presented a set of applicable algorithms and a new software tool for concurrent segmentation of images from different imaging modalities. The underlying principle in this work is to combine complementary information from different imaging sources for better understanding of the nature of the imaged object relevant to the depicted clinical task. This would result in a better target definition in radiotherapy treatment planning of cancer by integrating anatomical and physiological information to decide the target extent, and better classification of different tissue types from multi-spectral MR images in cardiac diagnosis routines. The multiple images to be integrated into such a framework need not to be from different image modalities. They could be from the same image modality but with different acquisition protocols (e.g., different MRI pulse sequences), or from the same acquisition protocol but at different times (e.g. 4D-CT images).

In many situations, one segmentation method may not perform very well. Different segmentation algorithms may perform better for different tissue types, different image gradient situations, different imaging modalities, or even different regions of the same image. For example, thresholding method may perform better than a sophisticated automatic algorithm to segment bony structures in CT images. It is often desirable to use different segmentation methods in a single image segmentation task so that different methods can be evaluated and the best one is selected for the task. This strategy is embedded in the design philosophy of the MIASYS software tool.

There are many different segmentation algorithms with different advantages and disadvantages. We have only presented three basic categories of algorithms to demonstrate the concept. There are certainly other automatic algorithms that could be generalized to support such a multiple image segmentation framework.

The MIASYS software tool is intended to demonstrate these extended algorithms, and to support and test the idea of combining different segmentation methods to ultimately achieve better segmentation results. The two presented examples have demonstrated that MIASYS and the extended algorithms are capable of performing well in difficult diagnostic and therapeutic radiological applications.

MATLAB is not the most computationally efficient environment. However, most of the implemented algorithms, programmed with MATLAB, are fast enough, in particular if the users can effectively define ROI and crop images to reduce the image dimensions using the available tools in the software. Therefore, computation speed is not a limiting factor for our software tool.

A larger issue is that some automatic algorithms use many user configurable parameters and users cannot easily choose the best parameter values. We have chosen default values for the parameters based on our experience to be used as initial guesses by user. However, in many scenarios these parameters may still need to be tweaked by the users to achieve optimal results.

Validation of the final results is one of the most challenging tasks in medical image segmentation applications. It could be done by comparing the segmentation results to histological data if such data are available and applicable. Results can also be compared to other “golden” standards, such as structure contours manually drawn by experts. However, such comparisons are often affected by other issues, for example, inter-observer variability. However, it is relatively safe to think about such automated methods as ‘second readers’ that would aid the users. This has been shown in many CAD applications to be a useful approach.

Image misalignments often occur. For this reason, we have included rigid registration algorithms in MIASYS. Issues related to registration of local deformations are not handled in the current version of the software but will be the subject of future work.

In our view, the integration of information from multiple image modalities is the most challenging task. We believe that the presented methodology and the software tool will provide an excellent platform to help unravel the high-level relationships between different imaging modalities as perceived by experts. We have introduced a new weighting parameters approach to control the influence of each image in the multimodality image dataset. These weighting parameters should be determined according to user's experience and prior knowledge. However, this procedure may be too simplistic and this issue is still an open area for future research.

6. CONCLUSION

We have presented a framework for extending different single-modality image segmentation algorithms to support simultaneous multimodality image analysis tasks. In addition, we have designed and developed an interactive software tool "MIASYS" to demonstrate the proposed multimodality framework. The MIASYS tool allows the user to apply different segmentation methods at different steps so that advantages of the different methods could be combined and the overall segmentation accuracy could be improved. A promising utilization of the proposed methods and the accompanying software tool are demonstrated in the two presented clinical examples from the therapeutic and diagnostic radiology fields. These examples demonstrate that the proposed approaches could be valuable for handling difficult multimodality image analysis tasks in various medical imaging applications. MIASYS is intended to be an open source software tool to promote and advance research in the medical multimodality imaging analysis area. It is freely available by contacting the authors, and can be used for any application that is non-commercial and does not alter treatment or diagnosis.

7. REFERENCES

- [1] J. H. Rudd, K. S. Myers, J. Sanz, and Z. A. Fayad, "Multimodality imaging of atherosclerosis (magnetic resonance imaging/computed tomography/positron emission tomography-computed tomography)," *Topics in Magnetic Resonance Imaging*, vol. 18, pp. 379-88, Oct 2007.
- [2] A. D. King, "Multimodality imaging of head and neck cancer," *Cancer Imaging*, vol. 7 Spec No A, pp. S37-46, 2007.
- [3] A. R. Hsu, W. Cai, A. Veeravagu, K. A. Mohamedali, K. Chen, S. Kim, H. Vogel, L. C. Hou, V. Tse, M. G. Rosenblum, and X. Chen, "Multimodality Molecular Imaging of Glioblastoma Growth Inhibition with Vasculature-Targeting Fusion Toxin VEGF121/rGel," *J Nucl Med*, vol. 48, pp. 445-454, March 1, 2007 2007.
- [4] D. W. Townsend, "Multimodality imaging of structure and function," *Phys Med Biol*, vol. 53, pp. R1-R39, Feb 21 2008.
- [5] I. El Naqa, "Radiotherapy Informatics: Targeted Control," *Enterprise Imaging & Therapeutic Radiology Management* vol. 18, pp. 39-42, May 2008.
- [6] W. L. Smith, C. Lewis, G. Bauman, G. Rodrigues, D. D'Souza, R. Ash, D. Ho, V. Venkatesan, D. Downey, and A. Fenster, "Prostate volume contouring: a 3D analysis of segmentation using 3DTRUS, CT, and MR," *Int J Radiat Oncol Biol Phys*, vol. 67, pp. 1238-47, Mar 15 2007.
- [7] E. M. Toloza, L. Harpole, and D. C. McCrory, "Noninvasive staging of non-small cell lung cancer: a review of the current evidence," *Chest*, vol. 123, pp. 137S-146S, Jan 2003.
- [8] J. D. Bradley, C. A. Perez, F. Dehdashti, and B. A. Siegel, "Implementing biologic target volumes in radiation treatment planning for non-small cell lung cancer," *Journal of Nuclear Medicine*, vol. 45 Suppl 1, pp. 96S-101S, Jan 2004.
- [9] S. Milker-Zabel, A. Zabel-du Bois, M. Henze, P. Huber, D. Schulz-Ertner, A. Hoess, U. Haberkorn, and J. Debus, "Improved target volume definition for fractionated stereotactic radiotherapy in patients with intracranial meningiomas by correlation of CT, MRI, and [68Ga]-DOTATOC-PET," *International Journal of Radiation Oncology Biology Physics*, vol. 65, pp. 222-7, May 1 2006.
- [10] D. L. Pham, C. Xu, and J. L. Prince, "Current methods in medical image segmentation," *Annu Rev Biomed Eng*, vol. 2, pp. 315-37, 2000.
- [11] J. S. Suri, S. K. Setarehdan, and S. Singh, *Advanced algorithmic approaches to medical image segmentation : state-of-the-art applications in cardiology, neurology, mammography, and pathology*. New York: Springer, 2002.

- [12] T. S. Yoo, M. J. Ackerman, W. E. Lorensen, W. Schroeder, V. Chalana, S. Aylward, D. Metaxes, and R. Whitaker, "Engineering and Algorithm Design for an Image Processing API: A Technical Report on ITK - The Insight Toolkit," *Proc. of Medicine Meets Virtual Reality*, pp. 586-592, 2002.
- [13] X. Papademetris, M. Jackowski, N. Rajeevan, R. T. Constable, and L. Staib, "BioImage Suite: An integrated medical image analysis suite," *The Insight Journal*, 2005.
- [14] M. J. McAuliffe, F. M. Lalonde, D. McGarry, W. Gandler, K. Csaky, and B. L. Trus, "Medical Image Processing, Analysis & Visualization in Clinical Research," in *Proceedings of the Fourteenth IEEE Symposium on Computer-Based Medical Systems*: IEEE Computer Society, 2001.
- [15] M. D. Abramoff, P. J. Magelhaes, and S. J. Ram, "Image Processing with ImageJ," *Biophotonics International*, vol. 11, pp. 36-42, 2004.
- [16] I. El Naqa, D. Yang, A. Apte, D. Khullar, S. Mutic, J. Zheng, J. D. Bradley, P. Grigsby, and J. O. Deasy, "Concurrent multimodality image segmentation by active contours for radiotherapy treatment planning," *Med Phys*, vol. 34, pp. 4738-49, Dec 2007.
- [17] A. Sebbahi, A. Herment, A. de Cesare, and E. Mousseaux, "Multimodality cardiovascular image segmentation using a deformable contour model," *Computerized Medical Imaging and Graphics*, vol. 21, pp. 79-89, 1997.
- [18] J. Zheng, I. E. Naqa, F. E. Rowold, T. K. Pilgram, P. K. Woodard, J. E. Saffitz, and D. Tang, "Quantitative assessment of coronary artery plaque vulnerability by high-resolution magnetic resonance imaging and computational biomechanics: A pilot study ex vivo," *Magnetic Resonance in Medicine*, vol. 54, pp. 1360-1368, 2005.
- [19] U. Nestle, S. Kremp, A. Schaefer-Schuler, C. Sebastian-Welsch, D. Hellwig, C. Rube, and C.-M. Kirsch, "Comparison of Different Methods for Delineation of 18F-FDG PET-Positive Tissue for Target Volume Definition in Radiotherapy of Patients with Non-Small Cell Lung Cancer," *J Nucl Med*, vol. 46, pp. 1342-1348, August 1, 2005 2005.
- [20] S. Hu, S. Hu, E. A. Hoffman, and J. M. Reinhardt, "Automatic lung segmentation for accurate quantitation of volumetric X-ray CT images," *IEEE Transactions on Medical Imaging*, vol. 20, pp. 490-498, 2001.
- [21] A. K. Jain, M. N. Murty, and P. J. Flynn, "Data clustering: a review," *ACM Comput. Surv.*, vol. 31, pp. 264-323, 1999.
- [22] C. B. James, *Pattern Recognition with Fuzzy Objective Function Algorithms*: Kluwer Academic Publishers, 1981.
- [23] D. L. Pham, "Spatial models for fuzzy clustering," *Comput. Vis. Image Underst.*, vol. 84, pp. 285-297, 2001.
- [24] C. Weiling, C. Songcan, and Z. Daoqiang, "Fast and robust fuzzy c-means clustering algorithms incorporating local information for image segmentation," *Pattern Recogn.*, vol. 40, pp. 825-838, 2007.
- [25] M. R. Anderberg, *Cluster analysis for applications*. New York, NY: Academic Press, Inc., 1973.
- [26] J. A. Sethian, *Level Set Methods and fast marching methods: evolving interfaces in computational geometry, fluid mechanics, computer vision, and material science*, second ed. Cambridge: Cambridge University Press, 1999.
- [27] C. Xu, D. L. Pham, and J. L. Prince, "Image Segmentation Using Deformable Models," in *Handbook of Medical Imaging: Medical Image Processing and Analysis*. vol. 2, M. Sonka and J. M. Fitzpatrick, Eds.: SPIE (The International Society for Optical Engineering) Press, 2002, pp. 129-174.
- [28] G. Aubert, *Mathematical problems in image processing : partial differential equations and the calculus of variations*, 2nd ed. New York: Springer, 2006.
- [29] S. Osher and R. P. Fedkiw, *Level set methods and dynamic implicit surfaces*. New York: Springer, 2003.
- [30] M. Kass, A. Witkin, and D. Terzopoulos, "Snakes: Active contour models," *International Journal of Computer Vision*, vol. 1, pp. 321-331, 1988.
- [31] V. Caselles, R. Kimmel, and G. Sapiro, "Geodesic Active Contours," *International Journal of Computer Vision*, vol. 22, pp. 61-79, 1997.
- [32] T. F. Chan and L. A. Vese, "Active contours without edges," *IEEE Transactions on Image Processing*, vol. 10, pp. 266-277, 2001.
- [33] T. F. Chan, B. Y. Sandberg, and L. A. Vese, "Active Contours without Edges for Vector-Valued Images," *Journal of Visual Communication and Image Representation*, vol. 11, pp. 130-141, 2000/6 2000.
- [34] J. Shah, "Curve evolution and segmentation functionals: application to color images," in *Image Processing, 1996. Proceedings., International Conference on*, 1996, pp. 461-464 vol.1.
- [35] Y. Wu, D. Yang, D. Khullar, I. E. Naqa, and J. Deasy, "SU-FF-J-126: An Open-Source Radiotherapy Image Registration Toolkit Integrated with CERR," *Medical Physics*, vol. 34, p. 2397, 2007.

- [36] L. Ibanez, W. Schroeder, L. Ng, and J. Cates, *The ITK Software Guide*: Kitware Inc, 2005.
- [37] D. Mattes, D. R. Haynor, H. Vesselle, T. K. Lewellen, and W. Eubank, "PET-CT image registration in the chest using free-form deformations," *IEEE Transactions on Medical Imaging*, vol. 22, pp. 120-128, 2003.
- [38] G. Hermosillo, C. Chef'd'Hotel, and O. Faugeras, "Variational Methods for Multimodal Image Matching," *International Journal of Computer Vision*, vol. 50, pp. 329-343, 2002.
- [39] C. Tomasi and R. Manduchi, "Bilateral filtering for gray and color images," *International Conference on Computer Vision*, pp. 839-846, 1998.
- [40] A. Nieminen, P. Heinson, and Y. Neuvo, "A new class of detail-preserving filters for image processing," *IEEE Trans. Pattern Anal. Mach. Intell.*, vol. 9, pp. 74-90, 1987.
- [41] K. Zuiderveld, "Contrast limited adaptive histogram equalization," in *Graphics gems IV*: Academic Press Professional, Inc., 1994, pp. 474-485.
- [42] O. Salvado, O. Salvado, C. Hillenbrand, Z. Shaoxiang, and D. L. A. W. D. L. Wilson, "Method to correct intensity inhomogeneity in MR images for atherosclerosis characterization," *IEEE Transactions on Medical Imaging*, vol. 25, pp. 539-552, 2006.
- [43] L. R. Dice, "Measures of the Amount of Ecologic Association Between Species," *Ecology*, vol. 26, pp. 297-302, July 01, 1945 1945.
- [44] T. Beyer, D. W. Townsend, T. Brun, P. E. Kinahan, M. Charron, R. Roddy, J. Jerin, J. Young, L. Byars, and R. Nutt, "A combined PET/CT scanner for clinical oncology," *J Nucl Med*, vol. 41, pp. 1369-79, Aug 2000.
- [45] J. Bradley, W. L. Thorstad, S. Mutic, T. R. Miller, F. Dehdashti, B. A. Siegel, W. Bosch, and R. J. Bertrand, "Impact of FDG-PET on radiation therapy volume delineation in non-small-cell lung cancer," *International Journal of Radiation Oncology Biology Physics*, vol. 59, pp. 78-86, May 1 2004.
- [46] J. Hanley, M. M. Debois, D. Mah, G. S. Mageras, A. Raben, K. Rosenzweig, B. Mychalczak, L. H. Schwartz, P. J. Gloeggler, W. Lutz, C. C. Ling, S. A. Leibel, Z. Fuks, and G. J. Kutcher, "Deep inspiration breath-hold technique for lung tumors: the potential value of target immobilization and reduced lung density in dose escalation," *Int J Radiat Oncol Biol Phys*, vol. 45, pp. 603-11, Oct 1 1999.
- [47] B. Zangheri, C. Messa, M. Picchio, L. Gianolli, C. Landoni, and F. Fazio, "PET/CT and breast cancer," *European journal of nuclear medicine and molecular imaging*, vol. 31 Suppl 1, pp. S135-42, Jun 2004.
- [48] V. C. Cappendijk, K. B. Cleutjens, A. G. Kessels, S. Heeneman, G. W. Schurink, R. J. Welten, W. H. Mess, M. J. Daemen, J. M. van Engelshoven, and M. E. Kooi, "Assessment of human atherosclerotic carotid plaque components with multisequence MR imaging: initial experience," *Radiology*, vol. 234, pp. 487-92, Feb 2005.